The SHREAD gene therapy platform for paracrine delivery improves tumor localization and intratumoral effects of a clinical antibody

Sheena N. Smith[a,1,2], Rajib Schubert[a,b,1,3], Branko Simic[a,4], Dominik Brücher[a,4], Markus Schmid[a,5], Niels Kirk[a,6], Patrick C. Freitag[a], Viviana Gradinaru[b], and Andreas Plückthun[a,2]

[a]Department of Biochemistry, University of Zürich, 8057 Zürich, Switzerland; and [b]Division of Biology and Biological Engineering, California Institute of Technology, Pasadena, CA 91125

Edited by Rakesh K. Jain, Massachusetts General Hospital, Boston, MA, and approved March 18, 2021 (received for review September 10, 2020)

The goal of cancer-drug delivery is to achieve high levels of therapeutics within tumors with minimal systemic exposure that could cause toxicity. Producing biologics directly in situ where they diffuse and act locally is an attractive alternative to direct administration of recombinant therapeutics, as secretion by the tumor itself provides high local concentrations that act in a paracrine fashion continuously over an extended duration (paracrine delivery). We have engineered a SHielded, REtargeted ADenovirus (SHREAD) gene therapy platform that targets specific cells based on chosen surface markers and converts them into biofactories secreting therapeutics. In a proof of concept, a clinically approved antibody is delivered to orthotopic tumors in a model system in which precise biodistribution can be determined using tissue clearing with passive CLARITY technique (PACT) with high-resolution three-dimensional imaging and feature quantification within the tumors made transparent. We demonstrate high levels of tumor cell–specific transduction and significant and durable antibody production. PACT gives a localized quantification of the secreted therapeutic and allows us to directly observe enhanced pore formation in the tumor and destruction of the intact vasculature. In situ production of the antibody led to an 1,800-fold enhanced tumor-to-serum antibody concentration ratio compared to direct administration. Our detailed biochemical and microscopic analyses thus show that paracrine delivery with SHREAD could enable the use of highly potent therapeutic combinations, including those with systemic toxicity, to reach adequate therapeutic windows.

gene therapy | cancer therapy | PACT tissue clearing | 3D reconstruction | adenovirus

In the treatment of cancer, the last 20 y have seen a dramatic shift to the development of targeted therapies, which include biologics such as monoclonal antibodies (mAbs) and cytokines as well as small molecule inhibitors, offering higher degrees of cancer specificity than standard chemotherapies by targeting cancer-related pathways (1, 2). As mAbs are typically systemically administered, both on- and off-target toxicities can still occur. Systemic toxicities are even more of a concern for other biologics (e.g., cytokines or toxins) even when they are fused to a targeting moiety (3, 4)

Challenges in achieving adequate penetration of solid tumors by mAbs and other biologics combined with their inadequate and incomplete localization can make it highly challenging to achieve an acceptable therapeutic index in solid tumors. Despite their generally long half-lives, the need for repeat dosing can lead to acquired drug resistance due to rising and falling systemic drug concentration (5), and, particularly in combination therapies, nonoverlapping toxicity profiles can make maintaining therapeutic windows even more challenging (6, 7).

These limitations demand novel delivery systems that limit systemic drug exposure, enhance tumor penetration and retention, reduce costs, and are compatible with personalized therapeutic interventions via patient-specific biomarkers (8–10). Gene and cell therapies (e.g., CAR-T or hematopoietic stem cell therapy) (11–13) have rapidly emerged as new cancer treatment strategies with tremendous potential to overcome many of the limitations of conventional drugs by directly endowing cells or tissues in the patient with anti-cancer properties. Nonetheless, the enormous logistics required for patient-derived cell expansions are prohibitive for their use as standard treatments.

Viruses provide the most effective mechanisms to efficiently deliver genetic material to human cell subsets, and they have been exploited for a variety of cancer-therapeutic strategies (11). Our aim was to engineer a generic, nonreplicative (nononcolytic), targeted viral delivery platform that is capable of paracrine delivery. The fundamental concept is to infect tumor cells with genes encoding secreted therapeutic payloads, which are produced over an extended duration and only need to diffuse locally. We hypothesized that paracrine delivery could limit systemic drug exposure and

Significance

A challenge in cancer therapy is delivering high, consistent levels of therapeutics to tumors. Protein-based therapeutics (e.g., antibodies) are typically delivered intravenously and require multiple doses to get sufficient levels to traffic into tumors to exert an effect. Yet healthy tissues are also exposed to similar drug levels, which can lead to significant side effects. This study uses sophisticated three-dimensional imaging of transparent tumors to characterize a versatile gene therapy platform using adenovirus that solves this problem by producing drugs directly in the tumor. This approach increases the tumor-to-bloodstream level of a model antibody 1,800-fold in comparison to direct administration. Thus, this system could allow for the local production of highly potent drugs with greatly reduced risk of systemic toxicities.

Author contributions: S.N.S., R.S., and A.P. designed research; S.N.S., R.S., B.S., D.B., and N.K. performed research; D.B., M.S., P.C.F., and V.G. contributed new reagents/analytic tools; S.N.S., R.S., B.S., and A.P. analyzed data; and S.N.S. and A.P. wrote the paper

The authors declare no competing interest.

This article is a PNAS Direct Submission.

[1]S.N.S. and R.S. contributed equally to this work.

[2]To whom correspondence may be addressed. Email: s.smith@bioc.uzh.ch or plueckthun@bioc.uzh.ch.

[3]Present address: Research and Early Development, Roche Molecular Solutions, Pleasanton, CA 94588.

[4]B.S. and D.B. contributed equally to this work.

[5]Present address: Partnering, Roche Diagnostics GmbH, 82377 Penzberg, Germany.

[6]Present address: Translational Science, Numab Therapeutics, 8802 Wädenswil, Switzerland.

This article contains supporting information online at https://www.pnas.org/lookup/suppl/doi:10.1073/pnas.2017925118/-/DCSupplemental.

Published May 17, 2021.

circumvent challenges faced by systemic dosing in achieving sufficient tumor penetration, retention, and half-life.

Here, we report on an adenovirus serotype 5 (Ad5) virus platform for paracrine delivery, which has been engineered to overcome two fundamental challenges: 1) generic, exogenously added bispecific adapters are used to retarget Ad5 tropism to selectable specific surface biomarkers through the use of designed ankyrin repeat proteins (DARPins) (14, 15), and 2) a reversible shield based on trimerized single-chain variable fragment of an antibody (scFv) is employed that detargets virions from the liver and protects them from immune-based clearance mechanisms (16). The Ad5 used furthermore contains a mutation to ablate blood factor X binding to the viral capsid ($HAdV5^{HVR7}$). Taken together, these components form the SHielded, REtargeted ADenovirus (SHREAD) gene therapy platform that allows for the cell-specific delivery to genetic payloads to the tumor microenvironment.

In the present study, we used these tools in a first proof-of-concept study in HER2-overexpressing tumors grown orthotopically in the murine mammary fat pad (17) and produced the anti-HER2 therapeutic antibody trastuzumab (TZB) (18). In immunodeficient Fox Chase SCID-beige mice, TZB acts almost entirely directly on the tumor cells through receptor blockade; thus, anti-tumor effects are exclusively related to the concentration of mAb in the tumor (19, 20), thus constituting a particularly well-defined system.

To assess the efficacy of our paracrine-delivery strategy in comparison with the direct injection of the antibody, we measured tumor regression and antibody levels and carried out a detailed optical interrogation using passive CLARITY (PACT) tissue clearing, enabling high-resolution volumetric confocal imaging. Our optical interrogation strategy was used to examine the cell types infected, the level and distribution of secreted antibody within the tumor microenvironment and the liver, its effect on the tumor and vasculature, and the duration of production.

Our work shows the following: 1) successful production of antibodies with the correct biochemical and biophysical properties as the recombinant therapeutic by SHREAD; 2) targeted infection of the desired cell type in vivo; 3) continuous, sustained production of therapeutic levels of the biologic from within the tumor microenvironment with much lower amounts of the therapeutic diffusing into systemic circulation and with a much better ratio and duration than with the injected antibody; 4) local therapeutic effects visualized from the inside of the tumor, evidenced by formation of pores in the tumor and causing a highly porous vasculature; and 5) the inaugural implementation of PACT for characterization of tumors treated with a very versatile gene therapy.

Results

Adenoviral Paracrine Delivery of Biologics. Our SHREAD delivery platform uses nonreplicative adenoviral particles equipped with a targeting adapter (15) that recognizes a surface marker on tumor cells—in the present studies, HER2—and a reversible shield (16) to detarget them from the liver and protect them from immune-based clearance mechanisms (Fig. 1 *A* and *B*). Since we expect efficiency not to be high enough to transduce all of the tumor cells, we aim for secreted biologic payloads—in this case, a mAb encoded in the double-stranded DNA adenoviral genome—to hit neighboring tumor cells via paracrine effects (Fig. 1 *A* and *B*). We hypothesized that transduced tumor cells are then transformed into a therapeutic biofactory, leading to higher concentrations in the tumor microenvironment while much lower amounts diffuse into systemic circulation.

In the present study, we used the clinically approved anti-HER2 antibody TZB as a model mAb, as it can exert a growth-inhibiting effect directly on sensitive cell lines by signaling inhibition alone (19) and serves thus as a well-controlled system to explore this delivery strategy. TZB was encoded in the genome of a first-generation, nonreplicative adenovirus under the strong cytomegalovirus promoter, using the furin-2A sequence for coexpression of antibody heavy and light chains from a single open reading frame (Fig. 1*A*). This expression format allows for stochiometric expression of antibody chains, which, following signal sequence cleavage, cleavage by furin, and subsequent posttranslational modifications, indeed results in antibodies identical in protein sequence to their recombinantly produced counterparts (21–23).

The previously described bispecific adapter based on DARPins was used to both ablate the native adenoviral tropism to coxsackie adenovirus receptor (CAR) and confer HER2 specificity via the well-described HER2-specific DARPin G3 (15) (Fig. 1 *B*, *Top*; Fig. 1*C*). Additionally, we employed a previously described capsid-directed shield based on the anti-hexon antibody 9C12 (Fig. 1 *B*, *Bottom*) (16), and the decrease in infectivity is small on cell lines with high HER2 overexpression (Fig. 1*C*) (see *BT474 as an HER2-Positive Tumor Model*). As previously shown, the shield can greatly reduce antibody-dependent neutralization and liver tropism, significant for subsequent in vivo applications (16).

Antibody purified from cell-culture supernatants, following large-scale transduction of BT474 cells with full-length IgG1 TZB (Ad-TZB) and analyzed by electrospray ionization mass spectrometry (ESI-MS) following deglycosylation, had closely similar molecular properties to the recombinantly produced TZB in the clinic (i.e., Herceptin, Genentech) as evidenced by mass spectrometry (Fig. 1*D*) and functional tests (see *Transduced Tumor Cells Secrete Functional Therapeutic Antibodies*). For an extensive characterization of the glycosylation status of antibodies produced by malignant tissues, including TZB produced from BT474 cells and the potential impact on antibody effector functions, we refer to an earlier study of our group (21).

BT474 as an HER2-Positive Tumor Model. To determine an optimal tumor model for paracrine delivery studies, two HER2-positive tumor cell lines were assessed for their HER2 levels, transduction efficiency via the HER2-adapter, antibody expression levels, and TZB sensitivity in vitro. These cell lines included SKOV3ip, a human ovarian adenocarcinoma used in previous adenoviral retargeting and shielding animal studies (16), and BT474, a human mammary ductal carcinoma previously described to be highly HER2-addicted and thus sensitive to anti-HER2 therapy (17). Flow cytometry titrations revealed the highest surface HER2 levels for BT474; SKOV3ip was ∼33% lower, and the controls (human embryonic kidney cells [HEK293] and human lung carcinoma A549) were 1 to 2 orders of magnitude lower (*SI Appendix*, Fig. S1 *A* and *C*). Levels of the native adenovirus receptor CAR were highest in HEK293 cells, ∼57% and 67% lower in A549 and BT474 cells, respectively, and very low (∼100-fold lower) in SKOV3ip (*SI Appendix*, Fig. S1 *B* and *D*).

We determined the transduction efficiency both via CAR (i.e., naked adenovirus) and via HER2 (i.e., HER2 adapter–coated adenovirus) by transducing cells with a virus encoding a TdTomato reporter gene, and we assessed reporter expression by flow cytometry (Fig. 1*C*). The in vitro transduction efficiency corresponded to the surface levels of the targeted receptor (either native CAR or HER2), with the highest HER2 transduction levels (86%) achieved in BT474 cells. Higher transduction levels are observed for HEK293 independent of blocking or retargeting, even though this cell line expresses only very little HER2. This is due to the fact that first-generation Ad is able to actively replicate in HEK293 during the course of the experiment, as HEK293 cells provide missing viral replication components in trans (24).

To test efficacy of the antibody itself without any indirect effects, a cell line sensitive to the direct signaling inhibition by therapeutic payload was required. Cell proliferation assays (XTT) showed sensitivity to TZB only in BT474 cells (54% reduction in

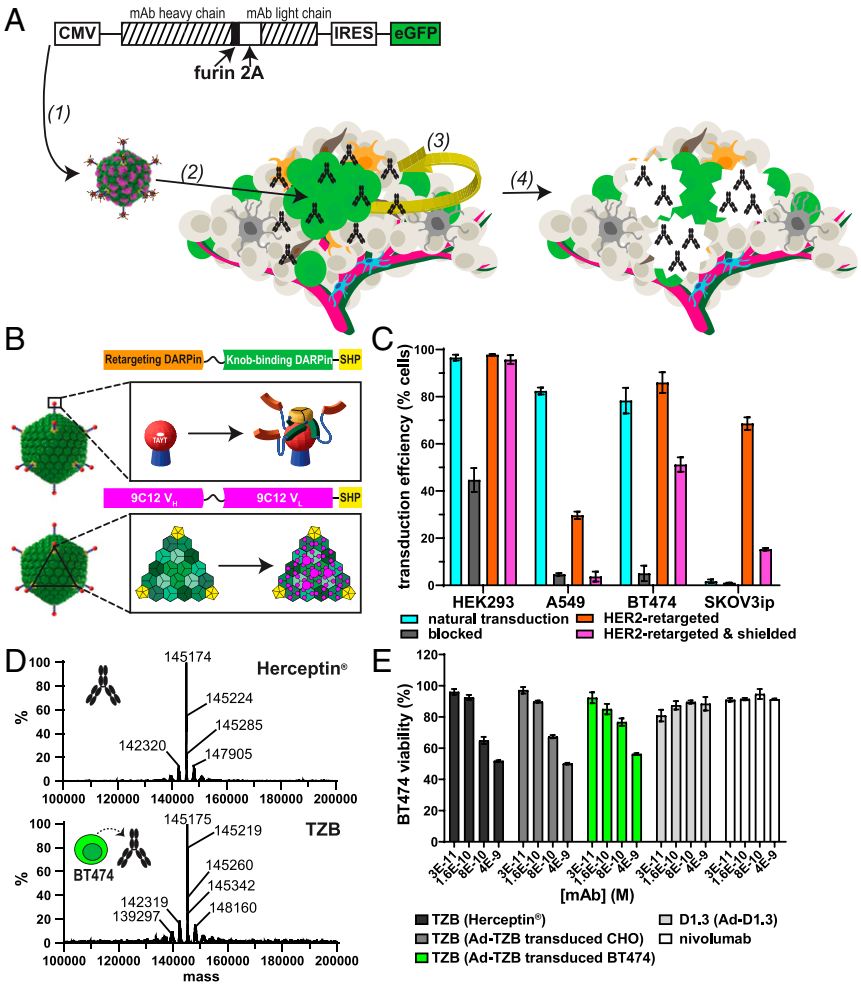

Fig. 1. Secretion of an anti-HER2 therapeutic antibody, TZB, by transduced tumor cells. (*A*) Schematic of paracrine delivery by SHREAD of a therapeutic antibody, TZB. The heavy and light chains of the therapeutic antibody are expressed from the cytomegalovirus (CMV) promoter using a furin-2A site, which leads to stochiometric expression of secreted chains via a previously described ribosome "skipping" mechanism and correct trimming of the heavy chain (22, 23, 49). Transgenes encoding the therapeutic antibody, TZB, and a transcriptionally coupled eGFP reporter are packaged into the genome of the SHREAD gene therapy platform, which consists of a retargeted and shielded Ad5 that is specific for the tumor surface antigen, HER2 (*1*) (15, 16). Upon administration of the virus, a subset of tumor cells is transduced via HER2 (green cells*; 2*) and acts of a therapeutic biofactory, secreting antibodies (black) in a paracrine fashion from within the tumor microenvironment where they diffuse locally (yellow arrow; *3*). The secreted antibody then exerts therapeutic effects directly on the tumor (e.g., by the formation of pores; *4*). (*B*) Schematic of a bispecific DARPin adapter that blocks the natural tropism of Ad5 while redirecting specificity to the chosen cell-surface biomarker (*Top*) (15). The Ad5 knob-binding module (orange) with SHP trimerization module (yellow), a protein from phage 21, is fused to a retargeting module (green) that allows for specific transduction of tumors expressing biomarkers for which it is specific (e.g., HER2). Schematic of the engineered trimeric protein-based "shield" that is coated on the Ad5 capsid (*Bottom*). The shield (magenta) binds spanning the threefold symmetry axes between neighboring pentameric hexon proteins on the viral capsid as previously described (16). Together with the retargeting adapter, it comprises the SHREAD gene therapy platform, which allows for improved tumor specificity and prevention of liver- and immune-based clearance mechanisms in immunodeficient mouse models (16). (*C*) Transduction of cell lines in vitro via the naked virus (natural, cyan), blocked virus (by a retargeting adaptor without the targeting DARPin, gray), HER2-retargeted virus (without shield [orange] and with shield [magenta]). Transduction is measured with a reporter virus that expresses fluorescent TdTomato by flow cytometry. Error bars represent SD for $n = 3$ replicates. (*D*) ESI-MS of commercially produced Herceptin (Genentech; *Top*) and TZB purified from culture supernatants of transduced BT474 cells (*Bottom*) following treatment with PNGase F and dihtiothreitol (DTT). Both show very similar profiles. (*E*) XTT of BT474 cells treated with recombinant TZB (Herceptin, Genentech, black), TZB purified from culture supernatants of CHO (dark gray) or BT474 (green) cells transduced with Ad5-TZB or with Ad-D1.3 (light gray), or a recombinant control antibody (anti-human PD1 antibody, nivolumab, Opdivo, BMS, white). Error bars represent SD for $n = 3$ replicates.

viability). As a further control, BT474 was not sensitive to an unrelated antibody, nivolumab (*SI Appendix*, Fig. S1 *E* and *F*). Accordingly, BT474 cells were selected as a tumor model for in vivo paracrine-delivery studies to observe effects directly caused by the secreted protein.

Transduced Tumor Cells Secrete Functional Therapeutic Antibodies. First-generation adenovirus (16) encoding Ad-TZB or a humanized isotype control (Ad-D1.3) were generated with high purity, as assessed by electron microscopy (*SI Appendix*, Fig. S2*A*), and at high titers, as determined by absorption measurements and infectivity assays (*SI Appendix*, Fig. S2*B*). To determine whether cells transduced with these viruses produced functional antibodies, a panel of cell lines was transduced in vitro with each virus with the same multiplicity of infection (MOI), and cell supernatants were analyzed 72 h later via an antigen capture enzyme-linked immunosorbent assay (ELISA) to determine the amount of secreted antibody that binds to target (*SI Appendix*, Table S1). To approximate yields per producing cell, the antibody amounts were normalized to the transduction efficiency, as determined by eGFP

reporter expression via flow cytometry, and they ranged from 3.37 to 24.7 and 7.09 to 154 pg per transduced cell for TZB and D1.3, respectively, 72 h posttransduction. Notably, these values are in the range of antibody production yields from Chinese hamster ovary (CHO) cells, which yield ~20 pg per cell per day (25).

TZB purified from Ad-TZB–infected BT474 cell supernatants not only showed closely similar mass spectra (see above) but could also induce similar growth inhibition as recombinant Herceptin or purified TZB from CHO cells transduced with the same Ad5 construct when applied to fresh BT474 cells, indicating that tumor cells were still sensitive to the autocrine (and paracrine) effects of the antibody they produced (Fig. 1*E*).

Paracrine Delivery of TZB Leads to Delayed Tumor Outgrowth In Vivo. Fox Chase SCID beige mice bearing BT474 orthotopic xenografts were treated with HER2-retargeted and shielded viral particles (1×10^8 ivp Ad-TZB or Ad-D1.3) or recombinant Herceptin (200 μg per dose) for a total of three doses (Fig. 2*A*). Tumor volumes were monitored for 60 d posttreatment initiation or until mice reached euthanasia criteria (Fig. 2*B*). No indications of acute toxicity were seen in any treatment groups as indicated by visual inspection of mice and by frequent weighing of mice during the first 2 wk of treatment (*SI Appendix*, Fig. S3*A*). Control Ad-D1.3– and phosphate-buffered saline (PBS)-treated mice showed the fastest tumor outgrowth, whereas Ad-TZB– and Herceptin-treated mice had delayed tumor outgrowth or

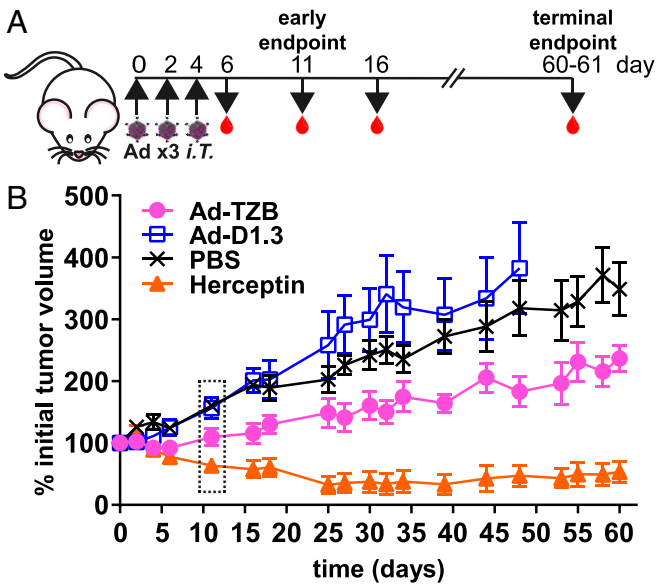

Fig. 2. Efficacy of Ad-TZB treatment of Fox Chase SCID beige mice bearing orthotopic BT474 xenografts. (*A*) Female Fox Chase SCID beige mice aged 7 to 8 wk were given a subcutaneous 0.36-mg 17β-estradiol implant and then engrafted 2 d later with 4×10^6 BT474 cells in Matrigel in the fourth mammary fat pad. Once tumors were established (50 to 250 mm^3), mice were treated intratumorally with 1×10^8 plaque-forming uits (PFU) Ad-TZB or control Ad-D1.3, 200 μg recombinant Herceptin, or PBS every other day for a total of three doses (i.e., on days 0, 2, and 4). Blood was collected on days 6, 11, 16 and at study termination (days 60 to 61). An additional cohort of mice was harvested at an interim time point on day 11. (*B*) Average tumor outgrowth measured for 60 d after initiation of treatment for Ad-TZB ($n = 6$), Ad-D1.3 ($n = 7$ until day 16, then $n = 6$ until day 48, when mice reached euthanasia criteria), PBS ($n = 7$), and Herceptin ($n = 7$). Error bars represent SE. The time point boxed in a dotted line represents the time point chosen for interim analysis (i.e., day 11). Statistical analysis was performed using linear regression of data using a mixed-effects model to account for variation between subjects as shown in *SI Appendix*, Fig. S3 *C* and *D*, and slopes were found to have nonoverlapping confidence intervals. Outgrowth plots for individual mice are shown in *SI Appendix*, Fig. S3*E*.

tumor regression, respectively. Following study termination, the mass of excised tumors was taken and compared to the pre-euthanasia volume measurements, and these showed a good linear correlation to each other with an R^2 of 0.85 (*SI Appendix*, Fig. S3*B*). Linear regression analysis was applied to data of Fig. 2*B* using a mixed-effects model, which showed that the slopes among groups had nonoverlapping confidence intervals (*SI Appendix*, Fig. S3 *C* and *D*). Complete tumor regressions occurred in two of seven Herceptin-treated mice (*SI Appendix*, Fig. S3*E*). Based on the tumor outgrowth rates, day 11 was selected as an interim time point to assess differences in concentration gradients and therapeutic effects in detailed imaging studies.

Imaging Cytometry of Optically Cleared BT474 Tumors. We previously developed the PACT imaging technology to image single florescent cells and single molecules in intact mouse tissue and bodies (26, 27). PACT imaging involves a combination of in situ and postextraction tissue labeling, preservation, and clearing. Here, we use PACT clearing in combination with volumetric confocal imaging to visualize and digitally reconstruct the tumor microenvironment to quantify the effect of the administered therapy (Fig. 3, *SI Appendix*, Fig. S4, and Movies S1–S5).

To investigate the cellular composition of our tumors, we first generated a TdTomato reporter cell line (BT474-TdTomato) with a lentiviral construct and selected transduced cells for moderate TdTomato expression by fluorescence-activated cell sorting (FACS) (*SI Appendix*, Fig. S5*A*). The cell line was further validated for showing similar responsiveness to TZB as the parental BT474 cell line via XTT assay (*SI Appendix*, Fig. S5*B*).

We engrafted an additional cohort of mice with BT474-TdTomato (Fig. 2*A*) to be harvested at both 11 or 61 d post-treatment initiation. Mouse tumors and liver tissues were prepared via PACT, leading to tissues that are rendered entirely transparent (Fig. 3) (27–29). For assessing the cellular composition, we optically interrogated these tumors harvested on day 11 using immunohistochemistry (IHC) staining and endogenous fluorophore expression from the BT474 cells. For all tumor tissues assessed, sections from both tumor and liver were analyzed to ensure proper vasculature staining and perfusion quality were achieved prior to further analysis (*SI Appendix*, Fig. S6).

Cells were classified as BT474 tumor cells if they expressed the TdTomato reporter gene and/or stained positively for human HER2. In untreated tumors, colocalization of TdTomato and HER2 staining occurred in 76% of tumor cells (*SI Appendix*, Fig. S7*A*). Nevertheless, 15% and 9.7% of the tumor cell population were only positive for either TdTomato or HER2 alone, suggesting that either expression levels of HER2 and TdTomato had become more heterogenous in vivo compared to in vitro (*SI Appendix*, Figs. S1*C* and S5*A*), or endogenous TdTomato expression and HER2 staining were, in some cases, under the detection threshold of the microscope.

To further classify the stromal subtypes, we used antibodies against a series of stromal markers for murine cell types anticipated to infiltrate the xenograft in the immunodeficient mouse model: von Willebrand factor (vWF) for endothelial cells, F4/80 for macrophages, and vimentin for fibroblasts (*SI Appendix*, Fig. S7 *B–H*).

Retargeted and Shielded Adenovirus Leads to Specific Transduction of Tumor Cells. To determine the specificity of tumor cell transduction conferred by the HER2-retargeting adapter in vivo, BT474-TdTomato tumor slices were examined in tumors treated with Ad-D1.3, which encodes an isotype control antibody with a transcriptionally coupled eGFP reporter (Fig. 1*A*). This construct allowed for the determination of transduction biodistribution at day 11 in the absence of antibody effects on the tumor.

We found that of the Ad-D1.3-transduced cells in the tumor, 93.7% were BT474 tumor cells (Fig. 4 *A* and *E*.), and the remaining

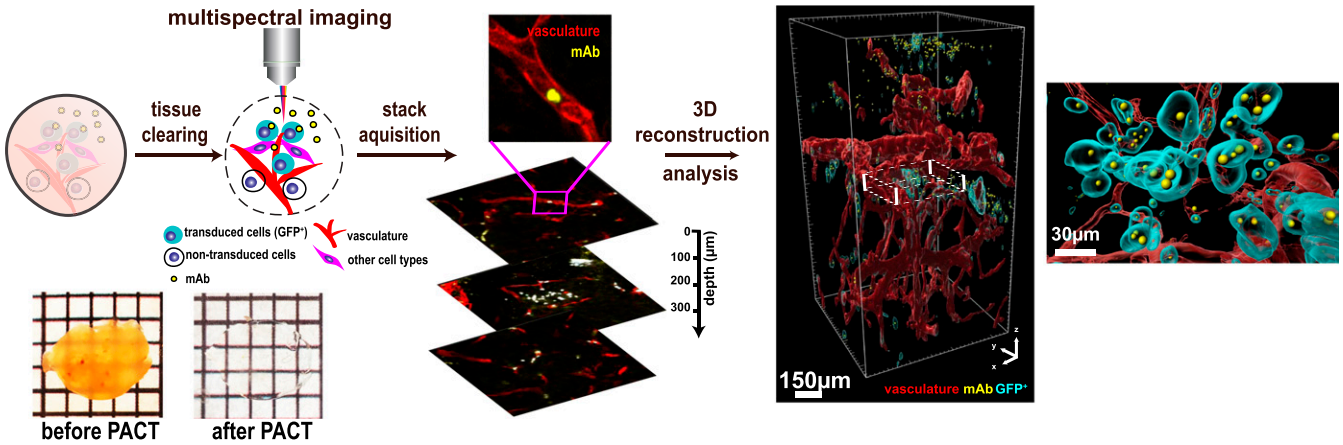

Fig. 3. Imaging cytometry workflow. The workflow consists of three modular steps: 1) PACT tissue clearing and labeling, 2) high-quality imaging using 3D confocal microscopy, and 3) 3D reconstruction and anatomical feature extraction of the vasculature, cell types, and paracrine-delivery strategy for statistical analysis. A tumor before and after PACT is shown on the bottom left.

6.33% were mouse-derived stromal cells, suggesting good specificity of the HER2-retargeted, shielded adenoviruses consistent with previous in vivo studies (16). To determine whether the GFP reporter signal was sufficient to be detected in tumors, Ad-D1.3–treated tumors were stained via IHC with an anti-GFP antibody to achieve a signal amplification. We found that the anti-GFP antibody signal colocalized with the GFP reporter in 90.8% of transduced cells, suggesting that less than 10% of the endogenous signal was below the detection threshold (*SI Appendix*, Fig. S7 *I* and *J*); no signal for GFP or anti-GFP could be detected in tumors treated with PBS only (*SI Appendix*, Fig. S7*K*).

To further classify the stromal subtypes that were transduced in the remaining 6.33% of the tumor, we used antibodies against a series of stromal markers for murine cell types anticipated to infiltrate the xenograft in the immunodeficient mouse model: vWF for endothelial cells (30), F4/80 for macrophages (31), and vimentin for fibroblasts (32). Due to low levels of costaining of tumor cells with these antibodies to varying degrees (*SI Appendix*, Fig. S7 *B–H*), quantifications of stromal cell characterizations were performed only on TdTomato-negative cells. We found that Ad-D1.3–transduced stromal cells predominantly (60.9%) costained for the macrophage marker F4/80 (Fig. 4 *C* and *G*).

Costaining with either vasculature (i.e., via Tomato-lectin, which binds vasculature glycoproteins) or vWF occurred in stromal cells at a rate of 10.2% (Fig. 4 *B* and *F*). Costaining for vimentin was observed in 11.3% of transduced stromal cells (Fig. 4 *D* and *H*). The remaining 10.2% of transduced stromal cells could not be classified. To summarize these data, transduction could be estimated to occur 93.7% in tumor cells, 3.7% in macrophages, 1.2% in vasculature cells, 1.0% in fibroblasts, and 0.5% in other cell types in the tumors overall (Fig. 4*I*); thus, the majority of untargeted cells transduced in the tumor microenvironment are macrophages.

Paracrine Delivery Leads to High Intratumoral with Significantly Lower Systemic Therapeutic Antibody Concentration. We then investigated the biodistribution of our paracrine delivery strategy of TZB in comparison to direct injection of the protein Herceptin. Visualization of tumors harvested at the early time point (i.e., day 11) allowed for the assessment of paracrine delivery at time points when 1) transduction has already occurred, 2) significant mAb and GFP reporter gene has accumulated, and 3) early therapeutic effects are seen yet without significant apoptosis due to autocrine effects of TZB (Fig. 5 and Movie S5). Visualization at the endpoint of the experiment (i.e., day 61), on the other hand, allowed for the assessment of sustained effects of the therapy over the course of the experiment. In both cases, we sectioned intact tumor tissues to 500-µm slices and subjected them to PACT for clarification. Slices representing the center of the tissues were stained with anti-human antibody conjugated with Alexa 594 and imaged in three dimensions (3D). We then rendered the reconstructed 3D volume and analyzed the relative amounts of antibodies within a defined volume. At both time points, day 11 and day 61, transduced tumor cells (cyan) are well distributed throughout the 3D section and are actively producing TZB mAb (yellow; Fig. 5) as indicated with the cyan arrows. The TZB mAb (yellow) secreted by the tumor cells diffused significantly throughout the tumor, where it is able to exert an autocrine and paracrine effect on BT474 cells (see below).

The liver serves as the primary site for mAb clearance (33); accordingly, measuring the TZB levels in liver tissue showed the systemic clearance of circulating mAb and allowed a comparison of paracrine delivery versus direct administration. To approximate the relative levels of antibodies in tumor and liver tissues, we imaged and compared 500-µm sections of tissue closest to the center of the tissue using the same staining and imaging parameters for both. The mAb signal was rendered using voxels in each tissue to show the relative antibody abundance in the tumor (Fig. 6*A*) versus the liver (Fig. 6*B*) of mice treated with PBS, direct administration of recombinant Herceptin, or paracrine-delivered Ad-TZB.

The occupied volume of TZB signal was quantified in tissues from various mice ($n = 3$ per group; Fig. 6 *C*, *Left*). Although these values do not allow for intratissue absolute concentrations of TZB to be determined, the relative ratio of tumor-to-liver signal in each mouse can be calculated and shows that the paracrine delivery approach leads to a much higher concentration ratio of tumor to liver compared to the administration of Herceptin protein (Fig. 6 *C*, *Right*). Notably, at the endpoint of the experiment (61 d), we could confirm by imaging that Ad-TZB–treated mice still had active TZB production in tumors in three of three Ad-TZB mice (i.e., by GFP reporter expression), and TZB could be detected in three of three Ad-TZB mice (i.e., by anti-human IgG) (e.g., *SI Appendix*, Fig. S8*A*). In an orthogonal approach to assess mAb-secretion levels at day 61, tumors from a subset of mice were lysed, and Western blots were performed using an anti-human κ-chain Fab fragment. Antibody signal was detectible in one of four Ad-TZB–treated mice and very faintly in one of five Ad-D1.3–treated mice 2 mo following the start of treatment (*SI Appendix*, Fig. S8*B*). Additionally, faint signals could be seen in two of three Herceptin-treated mice, suggesting residual mAb remains in the tumor following the administration of recombinant TZB.

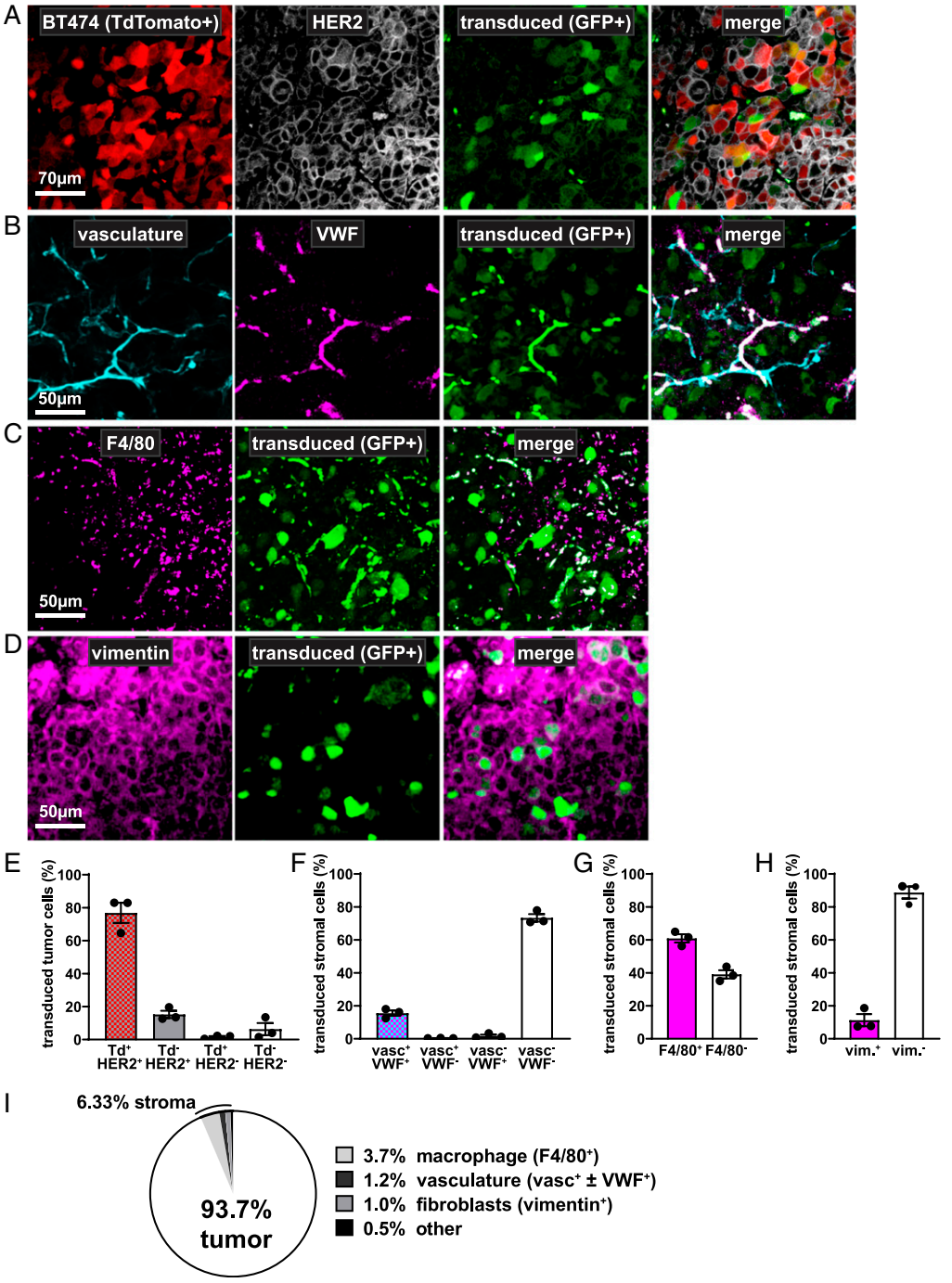

Fig. 4. Biodistribution of tumor-cell transduction. (*A–D*) Representative confocal microscopy images of tumor slices from mice treated with a virus that delivers an antibody isotype control (Ad-D1.3) and a transcriptionally coupled eGFP reporter (green). Slices originating from corresponding locations within tumors are costained with fluorescently labeled antibodies for various cell markers to determine the biodistribution of Ad transduction. (*A*) Transduction of BT474 tumor cells is shown by eGFP colocalization to BT474-endogenous TdTomato expression (red) and/or positive HER2 staining by IHC (white). Cells positive for eGFP alone are classified as transduced stroma and further characterized in the panels below. (*B*) Transduction of the tumor vasculature is indicated by GFP colocalization to lectin staining (cyan) and/or positive vWF staining (magenta). (*C*) Transduction of stromal macrophages is indicated by GFP colocalization with F4/80 staining (magenta). (*D*) Transduction of stromal fibroblasts is indicated by GFP colocalization with vimentin staining (magenta). (*E*) Transduction rate of tumor cells (Td^+Her2^+, Td^-Her2^+, and Td^+Her2^-) versus stromal cells (Td^-Her2^-) in Ad-D1.3–treated tumors. Values from $n = 3$ individual mice are shown as black dots; error bars represent SE (SEM). (*F–H*) Subclassification of transduced nontumor stromal cells. Tumor tissue was sectioned and stained for various markers via IHC (anti-F4/80, anti-vimentin, or anti-vWF) and used to further characterize the TdTomato-negative subpopulations. Values from $n = 3$ individual mice are shown as black dots; error bars represent SE (SEM). (*F*) Transduction rate of vasculature-associated cells ($vasc^+vWF^+$, $vasc^+vWF^-$, and $vasc^-vWF^+$) versus other stromal cells ($vasc^-vWF^-$). (*G*) Transduction rate of macrophages ($F4/80^+$) versus other stromal cells ($F4/80^-$). (*H*) Transduction rate of fibroblasts (vim^+) versus other stromal cells (vim^-). (*I*) Based on quantifications from the other panels, transduction biodistribution could be determined for the entire tumor. For simplification, F4/80-, vimentin-, and vWF-positive cells have been classified generally as macrophages, fibroblasts, or vasculature-associated cells, respectively.

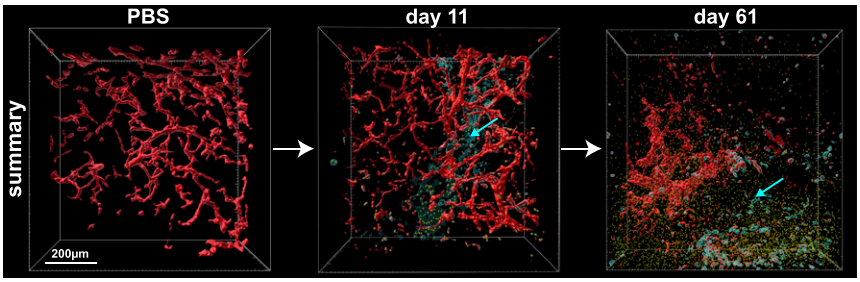

Fig. 5. Paracrine delivery of TZB. A summary of the paracrine effect of Ad-TZB treatment in a PBS tumor (*Left*), 11 d after treatment (*Middle*), and at the endpoint of treatment at 61 d (*Right*). Transduced cells (cyan cells, cyan arrows) secrete the antibody TZB (yellow spheres) locally where it accumulates and acts from within the tumor microenvironment. The tumor vasculature (red) can be seen being disrupted over time.

Residual mAb was also visible in two of two Herceptin-treated mice in confocal images (*SI Appendix*, Fig. S8*A*).

In addition to determining tumor and liver mAb levels, the concentration of TZB in circulation was determined in mice at various time points (i.e., at 6, 11, 16 and 60 d; Fig. 6*D*). Notably, the plasma concentrations of mAb from direct intratumoral (*i.T.*) administration on days 0, 2, and 4 of Herceptin remained high (micromolar level) through day 16 and were still detectible at nanomolar levels at 60 d in five of seven mice (gray bars, Fig. 6*D*). This is in the range of the published half-life described in the literature for TZB: 28 d in humans but as low as 7 d in mouse models (34, 35). In contrast, mAb levels in systemic circulation of Ad-TZB–treated mice were significantly lower (60- to 110-fold) at all time points and thus remained constant, consistent with TZB production from within the tumor being continuous (white bars, Fig. 6*D*).

Determining the relative levels of mAb achieved in tissues with paracrine delivery (i.e., Ad-TZB treatment) versus direct administration of recombinant Herceptin enabled the comparison of the two approaches: at day 11, we achieve 21-fold higher TZB in the tumor, 89-fold lower TZB in the plasma, and 2.2-fold lower TZB in the liver with paracrine delivery (Fig. 6*E*). In terms of therapeutic delivery, this corresponds to an 1,800-fold increase in the mAb concentration gradient from tumor to plasma and a 48-fold increase in the mAb concentration gradient from tumor to liver.

Paracrine Delivery Shows Increased TZB-Induced Pore Formation in the Tumor and in the Vasculature. To visualize how paracrine delivery of TZB might differ from direct administration in terms of therapeutic effect as visualized from inside the tumor as an orthogonal metric to overall tumor burden, two therapeutic parameters were measured in cleared tumors from immunodeficient mice: the formation of pores inside the tumor and the integrity of the tumor vasculature (Fig. 7).

Samples treated with Ad-TZB showed increased pore formation in the tumor compared to Herceptin-treated mice as indicated by the absence of DAPI nuclear staining in the core of tissue sections (Fig. 7*A*). Additionally, these tumors also showed increased vasculature disruption in comparison to Herceptin-treated mice, which increased from day 11 to 61 (Fig. 7*B*). Pore formation was quantified by determining the fraction of the tumor volume that is devoid of rendered DAPI-positive cells, excluding the margins of the tissue, at 11 and 61 d for each treatment group (Fig. 7*C*). At day 11, Herceptin- and Ad-TZB–treated tumors showed a four- and sixfold increase in pore volume compared to PBS tumors, respectively. At day 61, however, the average pore volume did not increase for Herceptin-treated mice anymore but increased 16-fold for the Ad-TZB–treated mice. Tumors treated with the control virus, Ad-D1.3, did not show significant pore formation in comparison to PBS-treated mice (*SI Appendix*, Fig. S9 *A* and *B*).

The anti-angiogenic properties of TZB have been well described in HER2-overexpressing tumor models (20, 36, 37). To quantify the anti-angiogenic effects, we determined the porosity index (pore volume/total occupied volume) of the vasculature at 11 and 61 d for each treatment group (Fig. 7*D*). At day 11, Herceptin- and Ad-TZB–treated tumors showed two- and sevenfold increased porosity index compared to PBS tumors, respectively. At day 61, the porosity index increased to fourfold and 16-fold in Herceptin- and Ad-TZB–treated tumors, respectively. Therefore, the porosity index became higher for Ad-TZB–treated tumors over treatment time. Tumors treated with the isotype control virus, Ad-D1.3, did not show significantly altered vasculature porosity in comparison to PBS-treated mice (*SI Appendix*, Fig. S9 *C* and *D*).

Together, these results indicate that tumors treated with the paracrine-delivered antibody (Ad-TZB) showed greater therapeutic effects from within the tumor than those treated directly with Herceptin despite showing a lower response in terms of overall tumor outgrowth (Fig. 2*B*).

Discussion

Our findings show that in situ production of a therapeutic antibody (termed "paracrine delivery") can lead to a superior localization within the tumor with only low amounts diffusing into systemic circulation in comparison to direct intratumoral administration of the recombinant therapeutic antibody. This leads to a significant therapeutic effect, evidenced by ablation of tumor cells leading to pores in the tumor and by causing a highly porous vasculature. Tissue clearing has enabled the visualization of the biodistribution and therapeutic efficacy of this delivery strategy by confocal 3D microscopy in detail. It revealed that antibody expressed upon paracrine delivery induces therapeutic effects (i.e., by pore formation and vasculature effects) from within the tumor, providing a strong rationale for the use of the SHREAD delivery platform for other applications in cancer therapy.

Despite measuring higher levels of TZB in the tumor with paracrine delivery at day 11 than in tumors treated with recombinant Herceptin, the overall tumor outgrowth indicated a higher objective response rate in Herceptin-treated mice with 2/7 complete remissions. As the mechanism of action of TZB is assumed to occur primarily through HER2-receptor blockade in this immunodeficient BT474 xenograft model (19), it is likely that the "burst" of concentration when recombinant Herceptin is injected intratumorally in bulk at the onset of treatment in the Herceptin-treated group leads to very high local concentrations capable of full receptor blockade and high initial response in tumor outgrowth. The remaining recombinant therapeutic then flows back into circulation, through which it is cleared over time, as supported by the relatively high antibody signal in the liver from Herceptin-treated mice at day 11. In contrast, the Ad-TZB–treated mice accumulate a large amount of antibody in the tumor from in situ production as shown at day 11, albeit much more gradually over

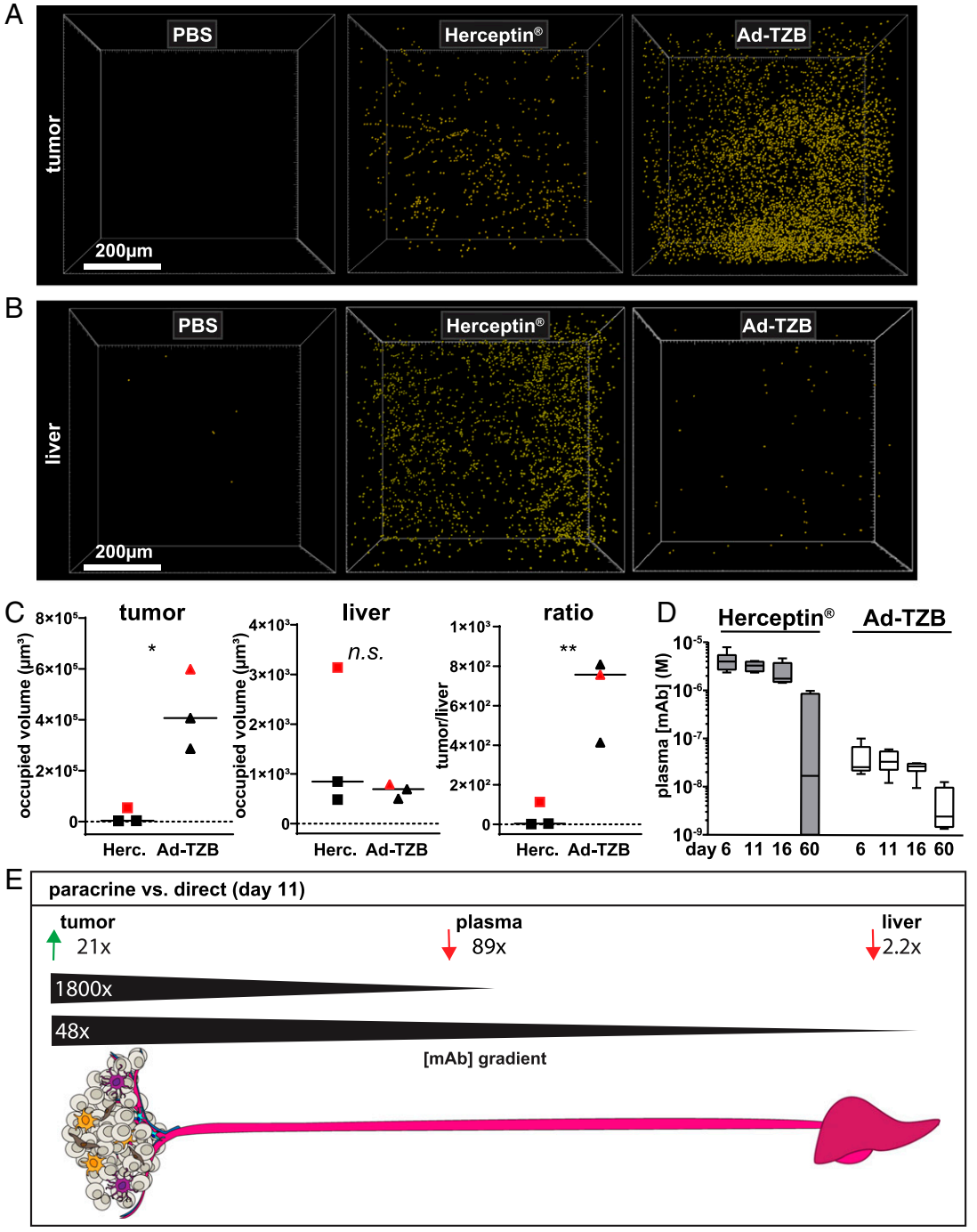

Fig. 6. Paracrine delivery leads to high intratumoral levels of antibody and lower drug systemic levels compared to direct administration of the protein. Relative levels of TZB (yellow spheres) within the tumor (*A*) and in the liver (*B*) following treatment with Ad-TZB versus direct administration of Herceptin. Images are shown from tissues of one of $n = 3$ mice. (*C*) Quantification of fluorescent intensity (occupied volume, μm^3) of tumor ($n = 3$, *Left*) and liver ($n = 3$, *Middle*) tissues stained for TZB with an anti-human antibody 11 d posttreatment with Ad-TZB or Herceptin. The ratio of tumor over the liver signal in each mouse is also shown ($n = 3$, *Right*). The images shown in *A* and *B* are indicated in plots with red squares (Herceptin) or red triangles (Ad-TZB). All values were normalized to background signal obtained from PBS mouse tissues. The solid black line represents the mean across the group; n.s. indicates $P > 0.05$, $*P \leq 0.05$, and $**P \leq 0.01$ from an unpaired *t* test performed using GraphPad Prism. (*D*) Average serum concentrations of systemic TZB 6, 11, 16, and 60 d after initiation of treatment determined by a HER2-capture ELISA and standard curve interpolation. Box plots represent five number summaries (min/Q1/med/Q3/max) for the antibody concentration for each mouse in the treatment group ($n = 6$ to 7). Data were analyzed using a two-way ANOVA with multiple comparisons using the Sidak method; *P* values for comparisons of Ad-TZB and Herceptin were <0.0001 (****) at day 6 and 11, <0.001 (***) at day 16, and not significant at day 60 (n.s.; $P > 0.05$) from an unpaired *t* test performed using GraphPad Prism. (*E*) Summary data comparing the amount of antibody reached in tumor, plasma, and liver with the paracrine-delivery strategy (i.e., Ad-TZB) compared with direct administration of the antibody (i.e., Herceptin) at day 11. Paracrine delivery leads to 21-fold higher antibody reached in the tumor with 89-fold less antibody in the plasma, thus increasing the overall concentration gradient from tumor to bloodstream 1,800-fold. For liver, paracrine delivery led to 2.2-fold less antibody in the liver, corresponding to a gradient effect of 48-fold from tumor to liver.

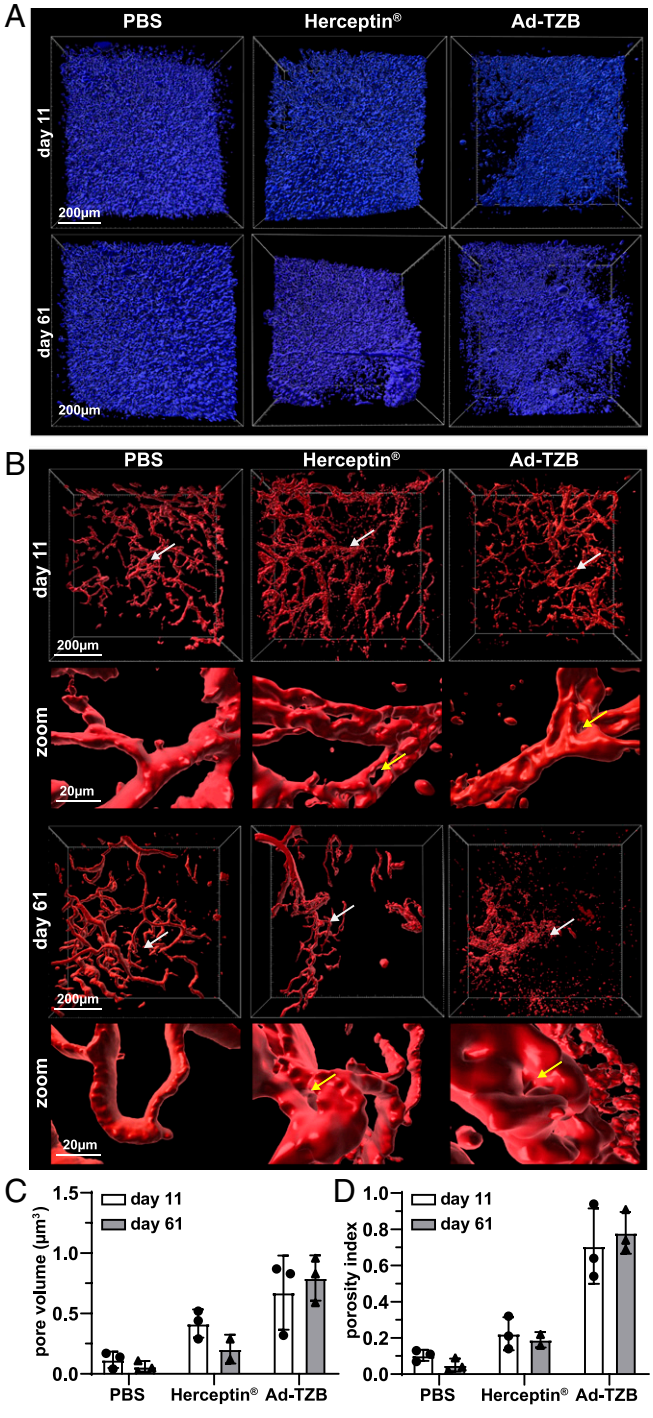

Fig. 7. Therapeutic efficacy of paracrine-delivered TZB in PACT-cleared HER2-positive BT474 xenografts. (*A*) Representative DAPI rendering (blue) showing tumor density of PBS- (*Left*), Herceptin- (*Middle*), and Ad-TZB–treated (*Right*) tumors at day 11 (*Top*) and day 61 (*Bottom*). (*B*) Representative vasculature rendering (red) of PBS- (*Left*), Herceptin- (*Middle*), and Ad-TZB–treated (*Right*) tumors at day 11 (*Top*) and day 61 (*Bottom*). The region indicated by the white arrows is shown at 10× higher magnification in the zoom panels below each overview image. Examples of pores are shown with yellow arrows. The vasculature images shown correspond to the same frames of samples shown in *A* above. (*C*) Quantification of total pore volume (μm^3) in tumors as determined by measuring the total area within the tumor that does not stain positively for nuclear DAPI staining, excluding tissue margins. All data points are for $n = 3$ mice, except Herceptin day 61 where $n = 2$. For this group, samples were limited at the endpoint, as complete regressions occurred in two of seven mice (of the five remaining, two were used for imaging and three to prepare lysates as shown in *SI Appendix*, Fig. S8*B*). Bars represent the means, and error bars indicate SDs; data points from individual mice are shown as black dots (day 11) or triangles (day 61). Data were analyzed with a two-way ANOVA with multiple comparisons and the Tukey post hoc test using GraphPad prism software (version 8.3.1). At day 11: PBS versus Herceptin (n.s.; $P > 0.05$), PBS versus Ad-TZB ($*P \leq 0.05$), Ad-TZB versus Herceptin (n.s.; $P > 0.05$); at day 61: PBS versus Herceptin (n.s.; $P > 0.05$), PBS versus Ad-TZB ($**P \leq 0.01$), Ad-TZB versus Herceptin ($*P \leq 0.05$). (*D*) Quantification of vasculature porosity index (vessel pore volume/total volume) for PBS-, Herceptin- and Ad-TZB–treated mice 11 d after treatment. As in *C*, all data points are for $n = 3$ mice, except Herceptin day 61 where $n = 2$. Bars represent the means, and error bars indicate SDs; data points from individual mice are shown as black dots (day 11) or triangles (day 61). Data were analyzed with a two-way ANOVA with multiple comparisons and the Tukey post hoc test using GraphPad prism software (version 8.3.1). At day 11: PBS versus Herceptin (n.s.; $P > 0.05$), PBS versus Ad-TZB ($***P \leq 0.001$), Ad-TZB versus Herceptin ($**P \leq 0.01$); at day 61: PBS versus Herceptin (n.s.; $P > 0.05$), PBS versus Ad-TZB ($****P \leq 0.0001$), Ad-TZB versus Herceptin ($**P \leq 0.01$).

time. This may not ever reach a concentration that is high enough to achieve complete blockade, particularly as the tumor grows. Notably, the BT474 tumor model has very high levels of HER2 amplified on the cell surface (1 to 2 million copies per cell), and TZB is generally classified as a cytostatic rather than apoptotic drug (38). It is likely that that the high concentrations required to see a large effect in this model represent an extreme case. Therefore, our detailed structural and mechanistic investigation of this approach may lead to choosing different optimal payload combinations in future treatments (see below).

Additionally, due to the nature of the comparison of the approaches (i.e., direct injection of large boluses of antibody versus localized production over time), it was not possible to precisely control the cumulative doses between the Ad-TZB and Herceptin treatment groups so that they were equal. Accordingly, we deliberately selected a rather high dose (3× 200 μg) for the Herceptin group for the purposes of this study and focused our analysis on comparing concentration gradients between various tissues and intratumoral effects at a set time point (day 11). Because of this high initial dose, sufficient quantities of antibody were still present in the tumor in Herceptin-treated mice in a similar range of those that had accumulated in the Ad-TZB mice at the midpoint analysis of 11 d, allowing for a comparison. Future studies will investigate how dosing can be better controlled across different delivery approaches.

In addition to assessing biodistribution of the mAb therapeutic, the identity of transduced cells following delivery with the SHREAD gene therapy platform could also be determined in these imaging experiments. We found that transduction occurred in BT474 tumor cells with 93.7% efficiency with the HER2-retargeted and shielded Ad-TZB, demonstrating the functionality of the adapter approach (15). The remaining cells transduced consisted of murine-derived stromal F4/80-positive macrophages (3.7%), vasculature-associated cells (1.2%), and fibroblasts (1.0%). Previous work from our group in a different xenograft model (i.e., RAG1 mice bearing subcutaneous $EGFR^+$ A431 tumors) qualitatively showed that, while again the desired tumor cells were predominantly transduced, murine fibroblasts were transduced to a small extent as a result of off-targeting, although this was not thoroughly quantified prior to the current study (16, 39). Nevertheless, it is important to mention that, since the therapeutic drugs are secreted, low amounts of expression by tumor stromal cells can still contribute to the therapeutic effect. In fact, retargeting adapters that deliberately target stromal cell markers are currently under development, as production in stromal cells would protect producer cells from the autocrine effects of the therapeutic over time. Stromal cells could even serve as a more productive

therapeutic production site in stroma-rich tumors such as pancreatic cancers, where the stroma can comprise >90% of the tumor volume (40). Although many targeting possibilities exist by the modular adapter strategy (15), payload specificity and potency will likely dictate what cells should be best targeted and what level of off-target or off-tissue transduction is acceptable. Furthermore, the use of inducible and/or tissue-specific promoters may provide an additional layer of specificity.

The tumor-to-plasma protein concentration ratio achieved is 1,800-fold higher for paracrine delivery by SHREAD versus direct administration of the therapeutic protein, and it is 48-fold higher for the tumor-to-liver concentrations. Furthermore, since the agent is produced continuously, this strategy could be of particular importance in establishing adequate therapeutic windows for therapeutics that are otherwise unavailable for cancer therapy. These include 1) narrow therapeutic index drugs and/or those otherwise "too toxic" for systemic therapy, such as costimulatory agonists or proinflammatory cytokines; 2) biologics with unacceptably short half-lives or those that require a concentration gradient for immune-cell recruitment, such as chemokines and cytokines; 3) complex therapeutic combinations aimed to collectively reshape the tumor microenvironment that might otherwise have noncompatible or nonoverlapping toxicity profiles; and 4) biologics that have highly complex posttranslational modifications and/or are too costly to produce recombinantly (41, 42). In particular, paracrine delivery could be massively advantageous in the delivery of immunotherapeutics for which localized production could add a layer of specificity significantly reducing systemic immune-related adverse effects. Moreover, the generic nature of retargeting via exogenously added bispecific adapters, shielding via viral epitope masking, and payload delivery via ligation-less assembly of payload cassettes allows for the testing of promising combinations in semihigh throughput and are compatible with personalized medicine approaches.

Our previous biodistribution studies have shown that the combination of retargeting and shielding could drastically improve tumor-to-liver transduction ratios not only when administered intratumorally (99.98% tumor to 0.01% liver) but also intravenously (70.9% tumor to 29.1% liver), albeit with a lower total level in the tumor with the intravenous route of administration (16). In the current study, we have used the intratumoral route to reach optimal specificity and overall transduction levels in the tumor for proof of concept; however, it should be possible to use intravenously administered viruses for paracrine delivery of suitable payloads, i.e., where high transduction levels in the tumor are not required, but where the better tumor-to-tissue ratios can be exploited (see above). Additionally, further engineering of the capsid shield to further reduce liver tropism, inclusion of additional capsid protein mutations that reduce transduction via secondary receptors (e.g., deletion of the Arg-Gly-Asp motif in the penton) (43), and/or pretreatment with angiogenesis inhibitors (e.g., bevacizumab) to increase tumor perfusion and viral trafficking may further enhance transduction efficiency and reduce off-targeting of intravenously administered viruses (44). It is also of interest to investigate how various routes of administration might enable the use of the SHREAD platform for metastatic tumor models and whether it might be possible to install therapeutic biofactories at multiple metastatic sites.

Lastly, these studies emphasize the vast potential for the use of tissue clearing, 3D imaging, and feature reconstruction in the field of tumor biology and drug delivery. This study is an innovative and extensive examination of 3D tumor cell composition, identification of transduced cells, release of the therapeutic proteins, and structural effects in tumors treated with gene therapy. This approach was highly effective in detecting and segmenting features of paracrine delivery in our imaging data, yielding a binary mask for all effects of our therapeutic intervention in the mouse. This strategy could be useful in other tumor-biology applications in which spatial information is critical, such as studies of tumor penetration, immunosuppression, heterogeneity, tumor microenvironment, and therapeutic delivery. We believe that new technologies currently under development will soon extend the imaging possibilities even further in extending imaging depth, resolution of the optical system, and preventing optical crosstalk (e.g., by the use of lattice sheet microscopy that delivers superresolution microscopy in 3D), large volume light sheet microscopy, and new instrumentation that allows for imaging of up to 17 colors (45).

Methods

Antibodies. Antibodies used are described in *SI Appendix, Supplementary Methods*.

Cloning, Production, and Purification of Antibody-Encoding Viruses. The AdEasy Adenoviral Vector System (46, 47) was adapted for delivery of genes encoding TZB or an isotype control virus, huD1.3, as described in detail in *SI Appendix, Supplementary Methods*.

Cell Culture. The following cell lines were purchased from the American Type Culture Collection (ATCC): BT474 (ATCC HTB-20), HEK293 (ATCC CRL-1573), and A549 (ATCC CCL-185). The human ovarian carcinoma cell line SKOV3ip was kindly provided by Ellen Vitetta (University of Texas, Dallas, TX). Cells were cultured as described in *SI Appendix, Supplementary Methods*.

Protein Purification of Adenoviral Shield and Knob. The HER2-retargeting and control knob-blocking adapters were expressed and purified in *E. coli* as previously described (15). Endotoxin was removed from purified adapters using the Endotrap HD Endotoxin Removal System (Hyglos GmbH), and adapters were stored at −80 °C in endotoxin-free Dulbecco's PBS (DPBS, Millipore TMS-012-A). The adenoviral shield was purified in *Sf9* insect cells as previously described (16).

In Vitro Transduction. Cells were seeded in either 12- or 24-well plates in 1.0 mL or 0.5 mL volumes, respectively, for 24 h pretransduction at the following seeding densities: HEK293 at 1.0 to 1.5 × 10^5 cells/mL, A549 at 1.0 × 10^5, and BT474 and SKOV3ip at 3.0 to 4.0 × 10^5 cells/mL. Prior to infection, adenovirus was preincubated with retargeting adapter (10-fold molar excess to adenoviral fiber knob) and/or shield (fivefold molar excess to adenoviral hexon) for 1 h on ice in DPBS, and then 1 × 10^3 vp/cell was added to culture medium in the wells of 12- or 24-well plates in 50- or 25-μL volumes, respectively. Cells were incubated with virus for 4 h, then the virus-containing supernatants were removed and exchanged with fresh media. For experiments in which antibody secretion was measured from transduced cells in supernatants, the media was not exchanged. Cells were incubated at 37 °C, 5% CO_2 and >90% humidity for 72 h posttransduction prior to analysis. Cell supernatants used for ELISA were filtered through a 0.2-μm filter and stored at −20 °C.

Flow Cytometry. For reporter analysis of transduced cells, cells were washed with 0.5 mL DPBS per well, then detached by addition of 0.5 mL trypsin-EDTA solution (Sigma T3924) per well and incubation at 37 °C for 3 to 5 min. The trypsinized cells were transferred into 0.5 mL complete media, centrifuged at 300 × *g* for 3 min at 4 °C, and washed with 1.5 mL cold PBS containing 1% bovine serum albumin. Sample readings were acquired without cell fixation on an LSRII Fortessa flow cytometry with FACSDiva software (Becton Dickinson) using a high-throughput sampler, and data were analyzed with FCS Express 5 (De Novo Software).

Antibody Expression and Purification. The day prior to infection, 1.2 × 10^7 BT474 cells were seeded in 5 × 15 cm dishes to achieve 90% confluency the following day. For suspension CHO-S cells, the cell density was adjusted to 2.0 × 10^6 (CHO-S) cells/mL on the day of infection. BT474 cells were infected with 1 infectious viral particle (ivp) per cell of HER2-retargeted adenovirus, and CHO-S cells were infected with 10 ivp per cell of naked adenovirus. Cell supernatants were harvested and pooled 5, 10, and 15 d postinfection for adherent cells and 7 d after infection for suspension cells. For expression of the D1.3 mAb used as a control, CHO-S cells were transiently transfected with the viral precursor plasmid pShuttle-MCS1_huD1.3 with polyethyleneimine and collected 5 d after transfection (48). Cell supernatants were filtered through a 0.2-μm filter, loaded onto prepacked 1 mL Protein A columns (GE 17040201), washed with 10-column volumes of PBS, and antibodies were eluted with 0.1 M citric acid (pH 2.5). Samples with detectable

absorbance at 280 nm were pooled, dialyzed against PBS, and stored at −80 °C until usage.

ESI-MS. Nano ESI-MS analyses of the samples were performed on a Synapt G2_Si mass spectrometer, as described in *SI Appendix, Supplementary Methods*.

XTT. Cells were seeded in 96-well plates 24 h prior to addition of antibody (HEK293 and A549 at 2×10^3 cells/well, BT474 and BT474-TdTomato at 3.2×10^3 cells/well and SKOV3ip at 3×10^3 cells/well). Antibodies were added at the indicated dilutions to wells containing cells and incubated at 37 °C, 5% CO_2 and >90% humidity for 4 d. Cell proliferation was measured via XTT assay (NeoFroxx 1167TT000) according to the manufacturer's protocol. Absorbance was measured at 463 nm with a reference wavelength at 670 nm.

ELISA. Antigen-capture ELISAs were performed using immobilized HER2 extracellular domain (Sino Biological 10004-HOSH) or 1 μM hen egg lysozyme (Sigma L6876), as described in *SI Appendix, Supplementary Methods*

Tumor Engraftment. Female Fox Chase SCID beige mice (CB17.Cg-Prkdc^{sci-d}Lyst^{bg-J}/Crl) were obtained from Charles River Laboratories at 5 wk of age and allowed to acclimate to the facility at least 2 wk prior to experimentation as described in *SI Appendix, Supplementary Methods*. Two days prior to engraftment, mice were implanted with 0.36 mg 90 d release 17β-estradiol tablets (Innovative Research of America NE-121) using 10-gauge precision trochars (Innovative Research of America MP-182) according to the manufacturer's protocol following administration of analgesic Rimadyl (Zoetis) at 5 mg/kg subcutaneously 30 min prior and anesthetic inhalation of isoflurane (induction 4 vol %/O_2 and maintenance 1.5 to 2.5 vol %/O_2). Human BT474 and BT474-TdTomato cell lines were verified to be pathogen-free via comprehensive PCR testing for Federation of European Laboratory Animal Science Associations mouse pathogens (IDEXX Laboratories). Cells were washed three times in ice-cold DPBS, passed through a 70-μm cell strainer (SPL Life Sciences Ltd 93070), and mixed 1:1 with Matrigel (Corning 356237) prior to engrafting 4×10^6 cells in 50 μL in the right abdominal mammary fat pad (i.e., below the fourth nipple) using a 30-gauge insulin syringe (BD 037-7614) under anesthesia with inhaled isoflurane.

Xenograft Studies. Tumors were measured three times per week using calipers. Once tumors reached a volume of 50 to 250 mm^3 [*tumor volume* = *(width)*^{2} × *length*/2], mice were allocated to treatment groups by starting tumor size to achieve a mean tumor volume of 200 mm^3 (SD 80 mm^3) in each treatment group. Mice were treated intratumorally with 1×10^8 ivp of HER2-retargeted and shielded viral particles, recombinant Herceptin (200 μg per dose, Genentech), or PBS at 48-h intervals for a total of three doses. Tumor outgrowth was measured for 60 d after treatment using calipers every second day and were normalized to the starting tumor volume (% initial tumor volume). A subset of wild-type BT474 tumors were harvested 11 and 61 d after onset of treatment via perfusion-fixation for CLARITY and confocal microscopy to assess therapeutic efficacy. All mice bearing BT474-TdTomato xenografts were harvested 11 d after onset of treatment via perfusion fixation for CLARITY and confocal microscopy to assess biodistribution.

Blood Collection. Goldenrod animal lancets (5 mm, MEDIpoint GR-5MM) were used for submental collection of 100 μL blood from mice 6, 11, and 16 d after start of treatment directly into microcentrifuge tubes containing 2 μL 0.5 M EDTA solution (Invitrogen 15575-020). Upon study termination and for collection of naïve mouse plasma used for controls, larger volumes of blood (~0.5 mL) were collected by heart puncture into tubes containing 10 μL 0.5 M EDTA solution. Samples were mixed by inversion, then centrifuged at 2,000 × *g* for 10 min. Supernatants containing plasma were transferred into new tubes and frozen at −20 °C for ELISA.

Perfusion Fixation and Vasculature Preservation. Mice were given a lethal dose of 100 mg/kg ketamine and 10 mg/kg xylazine prior to transcardial perfusion fixation with heparinized PBS followed with 4% paraformaldehyde (PFA; Electron Microscopy Sciences 15714-S) as previously described (27). For vasculature labeling, mice were injected intravenously with 100 μg DyLight 649 labeled *Lycopersicon esculentum* lectin (Vector Laboratories DL-1178) ~15 min prior to perfusion fixation. Tumors and livers were excised, placed into histology cassettes, and submerged in 4% PFA for 8 to 12 h. Tissues were then washed with PBS three times (12 h each) and then stored in PBS containing 0.2% sodium azide. Tissues were left intact or embedded into 4% low-melting agarose in PBS (Alfa Aesar H26417) in histology molds (Sigma E6032) and sectioned into 500-μm slices using a Vibratome series 1000 sectioning system (Leica).

PACT Clearing. Fixed tissue sections were incubated in hydrogel monomer solution A4P0 (4% acrylamide in PBS) supplemented with 0.25% photoinitiator 2,2′-azobis[2-(2-imidazolin-2-yl)propane] dihydrochloride (Wako Chemicals VA-044) at 4 °C overnight. Following incubation, the samples in solution were degassed with nitrogen for 5 min and then incubated for 30 min at 37 °C to initiate tissue–hydrogel hybridization. After removing excess hydrogel from tissue via brief PBS washes, tissue–hydrogel matrices were transferred into 50-mL conical tubes containing 8% sodium dodecyl sulfate (SDS) in 0.1 M PBS (pH 7.5) and were incubated for 2 to 5 d at 37 °C with shaking depending on tissue size. Samples were then washed with PBS for 15 min 4 to 5 times and assessed for transparency either visually or on an illumination dock (REX Technologie GmbH).

PACT Immunohistochemistry. Cleared tissue samples were washed with 4 to 5 changes of PBS over 1 d to remove residual SDS, then samples were incubated with primary antibodies at a 1:200 dilution in IHC antibody incubation buffer (PBS containing 2% normal goat serum [Thermo 31873], 0.1% Triton X-100, and 0.01% sodium azide) at room temperature with shaking for 3 to 7 d. After primary staining, samples were washed four to five times in PBS and incubated with secondary antibodies (1:200 dilution in IHC antibody incubation buffer) at room temperature with shaking for 2 to 5 d. Samples were washed with four to five changes of PBS over 1 d, then incubated in Refractive Index Matching Solution (RIMS) (40 g Histodenz [Sigma D2158] in 30 mL 0.02 M phosphate buffer [Sigma P5244] with 0.01% sodium azide, pH adjusted to 7.5 with NaOH resulting in a final concentration of 88% Histodenz wt/vol) at room temperature until they became transparent. For nuclear staining, samples were placed in a 1-mg/mL solution of Hoechst 33342 stain (Thermo H3570) for 1 h followed by washout in PBS for 1 h. The tissues were then placed back into RIMS for 4 h prior to imaging. All steps were performed at room temperature. Antibodies used for IHC of cleared tissues are described in *SI Appendix, Supplementary Methods*

Immunohistochemistry for In Situ–Produced Antibodies and Injected Herceptin. Fixed tissue sections were incubated with secondary antibodies of either goat anti-human IgG-AlexaFluor 594 (Thermo A-11014) for wild-type tumors or AlexaFluor 555 (Thermo A-21433) for TdTomato tumors in a 1:200 dilution of IHC antibody incubation buffer. Antibody staining was performed at room temperature with shaking for 2 to 5 d. Samples were washed once with PBS for 15 min and then incubated in RIMS.

Confocal Microscopy. Cleared tissue samples were mounted in RIMS on microscope slides (Thermo J1800AMNZ) using 0.5-mm or 1-mm spacers depending on sample thickness (iSpacer, SunJin Lab IS011 or IS012, respectively) and borosilicate glass coverslips (VWR 631-0134). BT474-TdTomato tumor and liver slices were imaged by Leica Microsystems using a Leica TCS SP8 confocal microscope. Images were acquired with either a 10×/ 0.3 (working distance [w.d.] 13.0 mm) or with a 20× multi-immersion lens/0.80 (w.d 0.67 mm) with an imaged field of view of 600 × 600 μm of 500-μm-deep sections. Within a given parameter, all images were recorded at the same laser power and gain control. Intact BT474 wt tumors were taken using a Zeiss LSM 880 confocal microscope with either the Plan-Apochromat 10×/ 0.45 M27 objective (w.d. 2.0 mm) or a LD LCI Plan-Apochromat 25×/0.8 Imm Corr DIC M27 multi-immersion objective (w.d. 0.57 mm). After imaging, samples were stored in RIMS at room temperature.

Image Quantification and Data Visualization. Two-dimensional maximum intensity projections were computed using IMARIS (Bitplane). 3D computer reconstructions of nuclei (Movie S1), blood vessels (Movie S2), and GFP-expressing cells (Movie S3) were made using the surfaces module in IMARIS, while for rendering secreted antibodies for display purposes in figures, the spot-detector tool in IMARIS was used (Movie S4). Reconstructed parameters were analyzed for spatial distribution, points between GFP cells, vasculature, antibodies, and porosity of vasculature using published MATLAB (Mathworks) code in IMARIS. The colocalization module was used to assess transduction efficiency (i.e., by overlay of GFP signal to TdTomato and/ or anti-HER2 staining). Most of the statistical analyses were performed using Prism (version 7.0 for Mac OSX; GraphPad Software), in which the Mann–Whitney *U* test was used for all cross-correlations in Fig. 4 and *SI Appendix*, Fig. S7, while the analyses used in different panels in Figs. 6 and 7 are described in the figure legends. Pearson correlation coefficients and coefficients of determination were obtained in MATLAB (version 2017b).

Data Availability. All study data are included in the article and/or supporting information.

ACKNOWLEDGMENTS. We acknowledge Gery Barmettler and the Center for Microscopy and Image Analysis at the University of Zürich for assistance with transmission electron microscopy, Serge Chesnov and the Functional Genomics Center Zurich for assistance with mass spectrometry, Polina Zaytseva for assistance in cloning the Ad-TdTomato reporter virus, Karen Patricia Hartmann and Julien Weber for assisting with animal sample collection, Junho Hur (Kyung Hee University) for microscopy time, Gerard M. Coughlin and Alon Greenbaum (California Institute of Technology) for assistance with PACT clearing and vasculature staining protocols, Bernadetta Tarigan for animal study statistics consulting, and the following individuals for helpful discussions: Alfred Zippelius, Nicole Kirchhammer and Abhishek Kashyap (University Hospital Basel); Urs Greber, Maarit Suomalainen, and Birgit Dreier (University of Zürich); David Baltimore (California Institute of Technology); and Uwe Zangemeister (University of Bern). This research is supported by the Swiss National Science Foundation Sinergia Grant 170929 (to A.P.), National Cancer Institute of the NIH under Award Number F32CA189372 (to S.N.S.), the University of Zurich Forschungskredit 2017 ID 3761 (to D.B.), and the Vallee Foundation (to V.G.).

1. H. Kaplon, M. Muralidharan, Z. Schneider, J. M. Reichert, Antibodies to watch in 2020. *MAbs* **12**, 1703531 (2020).
2. S. Hoelder, P. A. Clarke, P. Workman, Discovery of small molecule cancer drugs: Successes, challenges and opportunities. *Mol. Oncol.* **6**, 155–176 (2012).
3. D. J. FitzGerald, R. Kreitman, W. Wilson, D. Squires, I. Pastan, Recombinant immunotoxins for treating cancer. *Int. J. Med. Microbiol.* **293**, 577–582 (2004).
4. D. Neri, Antibody-cytokine fusions: Versatile products for the modulation of anticancer immunity. *Cancer Immunol. Res.* **7**, 348–354 (2019).
5. E. Cruz, V. Kayser, Monoclonal antibody therapy of solid tumors: Clinical limitations and novel strategies to enhance treatment efficacy. *Biologics* **13**, 33–51 (2019).
6. M. Vanneman, G. Dranoff, Combining immunotherapy and targeted therapies in cancer treatment. *Nat. Rev. Cancer* **12**, 237–251 (2012).
7. H. Ledford, Cocktails for cancer with a measure of immunotherapy. *Nature* **532**, 162–164 (2016).
8. R. S. Riley, C. H. June, R. Langer, M. J. Mitchell, Delivery technologies for cancer immunotherapy. *Nat. Rev. Drug Discov.* **18**, 175–196 (2019).
9. P. Lamichhane *et al*., Novel delivery systems for checkpoint inhibitors. *Medicines (Basel)* **6**, 74 (2019).
10. L. Milling, Y. Zhang, D. J. Irvine, Delivering safer immunotherapies for cancer. *Adv. Drug Deliv. Rev.* **114**, 79–101 (2017).
11. X. M. Anguela, K. A. High, Entering the modern era of gene therapy. *Annu. Rev. Med.* **70**, 273–288 (2019).
12. N. P. Restifo, M. E. Dudley, S. A. Rosenberg, Adoptive immunotherapy for cancer: Harnessing the T cell response. *Nat. Rev. Immunol.* **12**, 269–281 (2012).
13. A. Shahryari *et al*., Development and clinical translation of approved gene therapy products for genetic disorders. *Front. Genet.* **10**, 868 (2019).
14. B. Dreier *et al*., Her2-specific multivalent adapters confer designed tropism to adenovirus for gene targeting. *J. Mol. Biol.* **405**, 410–426 (2011).
15. B. Dreier *et al*., Development of a generic adenovirus delivery system based on structure-guided design of bispecific trimeric DARPin adapters. *Proc. Natl. Acad. Sci. U.S.A.* **110**, E869–E877 (2013).
16. M. Schmid *et al*., Adenoviral vector with shield and adapter increases tumor specificity and escapes liver and immune control. *Nat. Commun.* **9**, 450 (2018).
17. R. Tamaskovic *et al*., Intermolecular biparatopic trapping of ErbB2 prevents compensatory activation of PI3K/AKT via RAS-p110 crosstalk. *Nat. Commun.* **7**, 11672 (2016).
18. G. D. Lewis *et al*., Differential responses of human tumor cell lines to anti-p185HER2 monoclonal antibodies. *Cancer Immunol. Immunother.* **37**, 255–263 (1993).
19. C. A. Hudis, Trastuzumab–Mechanism of action and use in clinical practice. *N. Engl. J. Med.* **357**, 39–51 (2007).
20. Y. Izumi, L. Xu, E. di Tomaso, D. Fukumura, R. K. Jain, Tumour biology: Herceptin acts as an anti-angiogenic cocktail. *Nature* **416**, 279–280 (2002).
21. D. Brücher, V. Franc, S. N. Smith, A. J. R. Heck, A. Plückthun, Malignant tissues produce divergent antibody glycosylation of relevance for cancer gene therapy effectiveness. *MAbs* **12**, 1792084 (2020).
22. A. D. Simmons *et al*., Local secretion of anti-CTLA-4 enhances the therapeutic efficacy of a cancer immunotherapy with reduced evidence of systemic autoimmunity. *Cancer Immunol. Immunother.* **57**, 1263–1270 (2008).
23. J. Fang *et al*., Stable antibody expression at therapeutic levels using the 2A peptide. *Nat. Biotechnol.* **23**, 584–590 (2005).
24. F. L. Graham, J. Smiley, W. C. Russell, R. Nairn, Characteristics of a human cell line transformed by DNA from human adenovirus type 5. *J. Gen. Virol.* **36**, 59–74 (1977).
25. F. M. Wurm, Production of recombinant protein therapeutics in cultivated mammalian cells. *Nat. Biotechnol.* **22**, 1393–1398 (2004).
26. V. Gradinaru, J. Treweek, K. Overton, K. Deisseroth, Hydrogel-tissue chemistry: Principles and applications. *Annu. Rev. Biophys.* **47**, 355–376 (2018).
27. J. B. Treweek *et al*., Whole-body tissue stabilization and selective extractions via tissue-hydrogel hybrids for high-resolution intact circuit mapping and phenotyping. *Nat. Protoc.* **10**, 1860–1896 (2015).
28. K. Y. Chan *et al*., Engineered AAVs for efficient noninvasive gene delivery to the central and peripheral nervous systems. *Nat. Neurosci.* **20**, 1172–1179 (2017).
29. B. Yang *et al*., Single-cell phenotyping within transparent intact tissue through whole-body clearing. *Cell* **158**, 945–958 (2014).
30. N. G. Ordóñez, Immunohistochemical endothelial markers: A review. *Adv. Anat. Pathol.* **19**, 281–295 (2012).
31. J. M. Austyn, S. Gordon, F4/80, a monoclonal antibody directed specifically against the mouse macrophage. *Eur. J. Immunol.* **11**, 805–815 (1981).
32. M. Nurmik, P. Ullmann, F. Rodriguez, S. Haan, E. Letellier, In search of definitions: Cancer-associated fibroblasts and their markers. *Int. J. Cancer* **146**, 895–905 (2020).
33. M. J. Eigenmann, L. Fronton, H. P. Grimm, M. B. Otteneder, B. F. Krippendorff, Quantification of IgG monoclonal antibody clearance in tissues. *MAbs* **9**, 1007–1015 (2017).
34. M. Pegram, D. Ngo, Application and potential limitations of animal models utilized in the development of trastuzumab (Herceptin): A case study. *Adv. Drug Deliv. Rev.* **58**, 723–734 (2006).
35. J. Chen *et al*., The efficacy of trastuzumab in animal models of breast cancer: A systematic review and meta-analysis. *PLoS One* **11**, e0158240 (2016).
36. A. Viloria-Petit *et al*., Acquired resistance to the antitumor effect of epidermal growth factor receptor-blocking antibodies in vivo: A role for altered tumor angiogenesis. *Cancer Res.* **61**, 5090–5101 (2001).
37. A. M. Petit *et al*., Neutralizing antibodies against epidermal growth factor and ErbB-2/neu receptor tyrosine kinases down-regulate vascular endothelial growth factor production by tumor cells in vitro and in vivo: Angiogenic implications for signal transduction therapy of solid tumors. *Am. J. Pathol.* **151**, 1523–1530 (1997).
38. G. D. Lewis Phillips *et al*., Targeting HER2-positive breast cancer with trastuzumab-DM1, an antibody-cytotoxic drug conjugate. *Cancer Res.* **68**, 9280–9290 (2008).
39. P. Agarwal, E. A. Gammon, A. M. Sajib, M. Sandey, B. F. Smith, Cell-surface integrins and CAR are both essential for adenovirus type 5 transduction of canine cells of lymphocytic origin. *PLoS One* **12**, e0169532 (2017).
40. D. Xie, K. Xie, Pancreatic cancer stromal biology and therapy. *Genes Dis.* **2**, 133–143 (2015).
41. C. Xu *et al*., Comparative safety of immune checkpoint inhibitors in cancer: Systematic review and network meta-analysis. *BMJ* **363**, k4226 (2018).
42. K. C. Conlon, M. D. Miljkovic, T. A. Waldmann, Cytokines in the treatment of cancer. *J. Interferon Cytokine Res.* **39**, 6–21 (2019).
43. N. Arnberg, Adenovirus receptors: Implications for tropism, treatment and targeting. *Rev. Med. Virol.* **19**, 165–178 (2009).
44. J. B. Wu, Y. L. Tang, X. H. Liang, Targeting VEGF pathway to normalize the vasculature: An emerging insight in cancer therapy. *OncoTargets Ther.* **11**, 6901–6909 (2018).
45. D. L. Coutu, K. D. Kokkaliaris, L. Kunz, T. Schroeder, Three-dimensional map of nonhematopoietic bone and bone-marrow cells and molecules. *Nat. Biotechnol.* **35**, 1202–1210 (2017).
46. J. Luo *et al*., A protocol for rapid generation of recombinant adenoviruses using the AdEasy system. *Nat. Protoc.* **2**, 1236–1247 (2007).
47. T. C. He *et al*., A simplified system for generating recombinant adenoviruses. *Proc. Natl. Acad. Sci. U.S.A.* **95**, 2509–2514 (1998).
48. D. L. Hacker *et al*., Polyethyleneimine-based transient gene expression processes for suspension-adapted HEK-293E and CHO-DG44 cells. *Protein Expr. Purif.* **92**, 67–76 (2013).
49. J. Fang *et al*., An antibody delivery system for regulated expression of therapeutic levels of monoclonal antibodies in vivo. *Mol. Ther.* **15**, 1153–1159 (2007).